VTT Technical Research Centre of Finland

Single-Track Laser Scanning as a Method for Evaluating Printability: The Effect of Substrate Heat Treatment on Melt Pool Geometry and Cracking in Medium Carbon Tool Steel

Antikainen, Atte; Reijonen, Joni; Lagerbom, Juha; Lindroos, Matti; Pinomaa, Tatu; Lindroos, Tomi

Published in:
Journal of Materials Engineering and Performance

DOI:
10.1007/s11665-022-06826-0

E-pub ahead of print: 04/04/2022

Document Version
Publisher's final version

JMEPEG
https://doi.org/10.1007/s11665-022-06826-0

1059-9495/$19.00

TECHNICAL ARTICLE

Single-Track Laser Scanning as a Method for Evaluating Printability: The Effect of Substrate Heat Treatment on Melt Pool Geometry and Cracking in Medium Carbon Tool Steel

Atte Antikainen, Joni Reijonen, Juha Lagerbom, Matti Lindroos, Tatu Pinomaa, and Tomi Lindroos

Submitted: 8 November 2021 / Revised: 16 February 2022 / Accepted: 26 February 2022

Nearly all commercially available alloys have been developed for manufacturing processes other than additive manufacturing. Most of those alloys are not suitable for laser powder bed fusion (L-PBF) processing due to the non-weldable nature of the alloys developed for casting, forging, and machining. Even some weldable alloys can be difficult to produce with L-PBF because the characteristics of L-PBF, such as highly concentrated heat input and the extremely high cooling rate, can lead to very high residual stresses and cracking. In order to speed up the development process of new alloys for additive manufacturing, a powder-free evaluation method was used to evaluate the materials processing window and susceptibility to cracking. Single tracks were scanned with an L-PBF machine onto H13 steel substrates. The substrate condition was varied, and its effect on melt pool geometry and cracking behavior was evaluated. The results clearly show that thermal history of the substrate influences its thermal conductivity, affecting melt pool volume. Melting point of the substrate was not found as significant factor as thermal conductivity on melt pool dimensions. Cracking type was noted to differ between substrates. If printability is assessed without powder, the substrate microstructure should be similar to rapidly solidified material. It is recognized that single-track tests are not adequate in terms of residual stress evaluation, but they can give valuable information about materials' melting, segregation, and micro-scale cracking behavior.

Keywords additive manufacturing, cracking, single track, thermal conductivity, tool steel

1. Introduction

The commercial additive manufacturing (AM) of steels is mainly focused on alloys with very low carbon content, such as maraging steel M300, precipitation hardened stainless steel 17-4PH, and stainless steel 316L (Ref 1-4). Even though some low carbon steels can be categorized as martensitic, there is a great variation in properties depending on the carbon content of martensitic steel (Ref 5). For example, the hardness of laser powder bed fusion (L-PBF) maraging steel M300 is between 580 HV (Ref 2) and 650 (Ref 6) in a heat-treated condition, whereas the hardness of H13 is much higher at from 650 HV (Ref 7) to 894 HV (Ref 8) for as-built samples. Other steel powder products are of course available on the market, but the associative factor between nearly all of these is the low carbon content, leaving the commercial ferrous material selection rather limited. The need to develop new and specific L-PBF alloys arises from this limitation. In particular, high-performance tool steels that are difficult to machine have raised interest in recent years. Typically, the performance of a tool steel relies on a hard, martensitic matrix reinforced with embedded carbides. Neither of these features are considered good for weldability, which shows in its poor processability in AM. Hardenable AM steels like 17-4PH and M300 gain their properties from precipitation hardening during post-processing, supported by the inherent hardness of the low carbon martensitic matrix. The hardness of the matrix could simply be improved by introducing more carbon into the alloy. Hence, there exists a need for a state-of-the-art higher carbon martensitic alloy that is also suitable for the L-PBF process.

One carbon-containing tool steel alloy that has been adopted in AM is W302 (Böhler), also known as H13 (AISI). H13 is a chromium hot work tool steel with a carbon content of approximately 0.4 wt.%. H13 has good dimensional stability through its hardening properties and resistance to cracking during heat treatment (Ref 9). AM of H13 has been investigated by several authors (Ref 8, 10-16), but the examination of cracking behavior is not covered thoroughly. It remains unclear why H13 is printable regardless of its medium carbon content, high hardenability, and non-weldable nature.

A single-track method for AM research has been studied before, both with and without powder. The transition from conduction to keyhole-mode melting was observed in Ti-Nb alloy by Roehling et al. when varying laser power (Ref 17). An

Atte Antikainen, Juha Lagerbom, Matti Lindroos, and **Tomi Lindroos**, VTT Technical Research Centre of Finland Ltd, Visiokatu 4, 33101 Tampere, Finland; **Joni Reijonen**, VTT Technical Research Centre of Finland Ltd, Kemistintie 3, 02150 Espoo, Finland; and **Tatu Pinomaa**, VTT Technical Research Centre of Finland Ltd, Vuorimiehentie 2, 02150 Espoo, Finland. Contact e-mail: atte.antikainen@vtt.fi.

Published online: 04 April 2022

Nb-Ti-Cr alloy was investigated using a single-track method by Guo et al., who found suitable processing parameters for creating single layers of that particular alloy on a titanium platform (Ref 18). Yadroitsev et al. found that a too high platform pre-heating temperature caused balling when using an 80 μm layer thickness with 316L stainless steel. They also concluded that scan speed has a higher and more predictable effect on processability than very high platform temperatures (Ref 19). Yadroitsev et al. have also studied single-track scans with relatively low laser power on various other materials. They concluded that high thermal conductivity caused a small processing window (Ref 20). Lee et al. used an open-source artificial intelligence (AI) toolbox to predict melt pool geometries in single-track L-PBF and found it easier to predict the melt pool in the substrate but found it more difficult in the powder due to powder motion (Ref 21). Ghosh et al. studied single tracks on Inconel 625 without powder to validate finite element method (FEM) simulations and found good agreement with the experimental results when operating in conduction mode without keyhole formation. They also presented a method to evaluate forming crystal morphology based on average temperature and the solidification rate (Ref 22). Aboulkhair (Ref 23), Aversa (Ref 24), and Wei et al. (Ref 25, 26) studied aluminum alloys using the single-track method. It was found in (Ref 23) that when the heat input is sufficient, the keyhole is formed rather easily in AlSi10Mg, leading to conical melt pools rather than half-circular melt pools in stable single tracks. Aversa et al. (Ref 24) studied AlSi10Mg and A357 aluminum alloys and suggested the origin of pores lies in the poor connection of adjacent scan tracks, and thus, they cannot be seen in single-track tests. Crack-free alumina single tracks have been made by Fan et al. (Ref 27), who also noted that sufficient heat input results in continuous tracks. Single tracks on titanium have been investigated by Baitimerov (Ref 28).

Even though previous studies clearly show that the single-track method is useful in investigating the features of L-PBF in a simplified manner, less focus has been placed on the influence of the substrate itself on the single-track scan results. Ignoring variations in the base material's microstructure and thermal behavior may result in faulty conclusions on materials printability. This work explores how the thermal history of H13 tool steel affects the single-track study results, by assessing the microstructure, melting point, and thermal conductivity of the substrate. The hypothesis of the melting point's impact is based on a study by Shingu and Ishihara where they reported that a stable phase always has a higher melting point than its metastable counterpart (Ref 29) and presumption that alloying elements that are not dissolved in the matrix do not affect its properties (Ref 30). Accordingly, it is presumed that the substrate heat treatment condition affects the melt pool geometry and cracking behavior, which shall be experimentally investigated herein.

2. Materials and Methods

2.1 Substrate Preparation and Heat Treatments

Table 1 shows the nominal and the optical emission spectroscopy (OES) measured compositions of the tested W302 (H13) hot work tool steel. The material was tested in cast state, in different heat treatment conditions, and as manufactured with L-PBF. Heat-treated and cast materials were cut from an as-received soft annealed 30-mm bar manufactured by Böhler and supplied by Sten & Co. Ltd. An L-PBF substrate was additively manufactured from H13 powder supplied by SLM Solutions GmbH and is denoted as *L-PBF substrate condition* in this paper. Heat-treated samples were quenched in oil and tempered in a nitrogen atmosphere. In order to study the response of a melt quenched microstructure on single-track scanning, copper mold casting of the alloy was constructed. An Indutherm vacuum casting machine VTC 800 V was used to produce cast substrates from the W302 (H13) bar feedstock. Although cooling as fast as in L-PBF was not accomplished, it was presumed that the cast microstructure would give information of the materials behavior, together with comparison to wrought samples. As shown in Table 1, the nominal composition of all the substrates is the same, but minor differences in the actual composition measured using OES can be seen between the Böhler W302 and SLM Solutions H13 feedstock. Sample substrate conditions are presented in Table 2.

Prior to single-track tests, all the substrates were blasted with ceramic beads to normalize the surface and have similar absorptivity of the laser for each substrate. After blasting, the substrates were cleaned with ethanol to remove residual particles, oil, and grease.

2.2 Single-Scan Track Test Setup

The single-track scan experiments were conducted using an SLM 125 HL L-PBF machine from SLM Solutions GmbH. The optical configuration consists of an IPG-YLR-400-SM fiber laser; a $f = 50$ mm, $D = 25$ mm collimator; a Scanlab Varioscan 40 focusing unit; and a Scanlab Intelliscan 25 galvanometer scanner with maximum 400 W nominal output power and a beam diameter of 80 $\pm$ 6 μm at focus. The scan system is controlled with a Scanlab RTC5 control board. In total, 29 single-scan tracks with a length of 8 mm were done on each substrate. Twenty-five of the tracks were produced with varying laser power P (100-400 W) and scanning speed v (500-900 mm/s) to produce various line energies, $E_l = P/v$. In addition, four tracks were produced with de-focused laser with parameters shown in Figure 1 shows the nesting of the single-scan lines on the substrate and the test setup. A special build plate was utilized for the placement of the substrates into the middle of the scan field. The platform pre-heating temperature was set to 30 °C. The build chamber was closed and purged with 99.999% instrument argon to produce an atmosphere with oxygen content below 0.1%. After purging, the changing of the substrates was done using a rubber glove integrated into the build chamber door of the SLM 125 HL system to avoid opening the chamber and having to purge with argon each time. Before scanning each substrate, the automatic gas control of the SLM 125 HL system was turned on to maintain a process pressure of 12 mbar above atmospheric pressure and the shielding gas flow circulation was activated. The shielding gas flow rate was controlled by adjusting the circulation pump speed from 0 to 100% and monitored by a flow meter in the inlet piping (a 40 mm diameter pipe) of the system. A gas flow speed of 4 m/s was set for the experiments, which corresponds to a volumetric flow of ~300 l/min and which is distributed along the width of the chamber. At the center where the samples were placed, this corresponds to a ~0.5 m/s flow velocity above the platform, as measured with exactly the same SLM 125 HL machine in the experiments by Reijonen et al.

Table 1 W302 and H13 composition in wt.%

	Fe	C	Cr	V	Mo	Si	Mn			
W302 Nominal (Ref 33)	Bal.	0.39	5.10	1.00	1.30	1.00	0.40			
W302 OES	Bal.	0.39	5.20	0.92	1.26	0.99	0.40			
SLM Solutions H13 OES	Bal.	0.40	5.18	1.11	1.50	1.02	0.38			
	Ni	**Cu**	**Al**	**Ti**	**Co**	**Nb**	**N**	**O**	**S**	**P**
W302 OES	0.31	0.16	0.006	0.004	0.036	0.024	0.008	0.006	0.004	0.022
SLM Solutions H13 OES	0.07	0.01	0.006	0.011	0.019	0.008	0.040	0.008	0.010	0.009

Table 2 Heat treatment conditions of the substrates

Sample	Treatment
Annealed	.
Quenched (Q)	15 min at 1080°C, Oil quenching
Quench & temper (QT)	15 min at 1080°C, Oil quenching, Tempering 2 h at 550°C
Cast	Copper mold cast, pouring temp ~1450°C, simulated cooling rate from 1500°C to 500°C was 61°C/s.
L-PBF	Laser powder bed fusion with SLM Solutions 125 HL

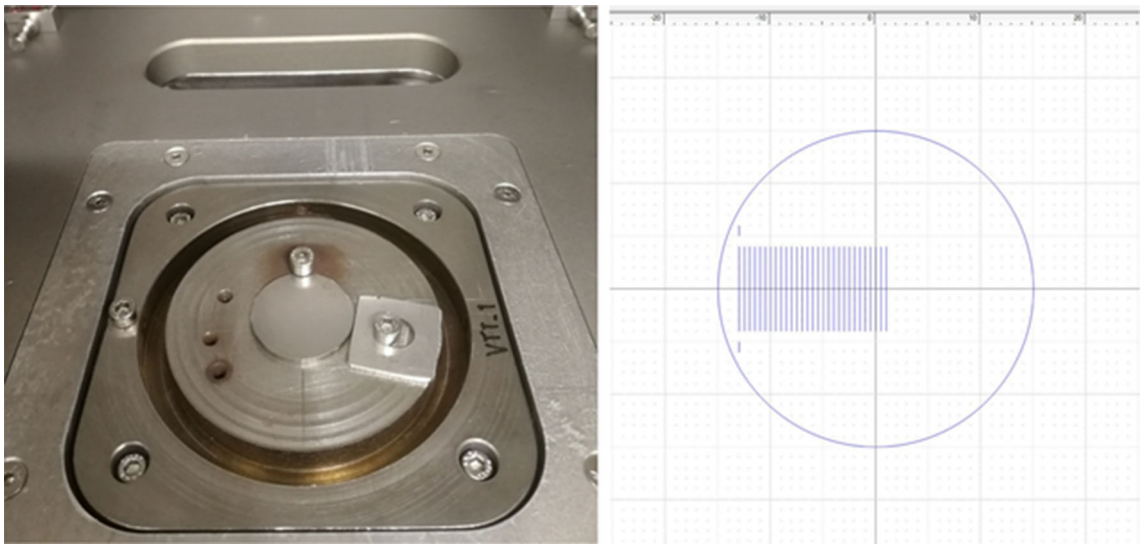

Fig. 1 Single-scan track test setup (on the left) and nesting (on the right) of the scan tracks on the substrate

(Ref 31) where it was shown that the shielding gas flow speed has an effect on the melt pool geometry of single-scan tracks.

2.3 Characterization

The substrates were characterized with X-ray diffraction (XRD) machine (PANalytical X'Pert Powder PW 3040/60) prior to single-track scanning. After scanning, the substrates were cut from the middle of the single-scan tracks, polished to mirror finish, and etched with Nital to reveal the microstructure and melt pool boundaries of the single-scan tracks. After first analysis of the cracking tendency, the samples were ground, polished, etched, and inspected again for improved reliability. Images were taken with optical microscope ZEISS Axio Observer Inverted Microscope. ImageJ (GNU license) software was used for measuring the melt pool dimensions from the single-scan tracks ex situ from the cross sections. Electron backscatter diffraction (EBSD) studies were performed with a Zeiss Crossbeam 540 scanning electron microscope (SEM) with an EDAX Hikari Plus EBSD detector. Vickers hardness (HV0.1) was measured across the melt pool for selected parameters.

2.4 Thermal Conductivity

Thermal conductivity of the substrates was measured with a Hot Disk 2500S thermal constants analyzer using 5465 sensor. The samples were cut into a 15-mm-thick and 30-mm-wide cylinders from the same bar as the single-track samples. Heat treatments were done similarly to the single-track samples, but dwell time at 1080 ºC was set to 40 min instead of 15 min to compensate for the increased thickness. Due to the small size of

the L-PBF substrate, another sample from the same print job was used for the thermal conductivity measurements. Measurement parameters were 1 s heating time, 400 mW heating power, and a fine-tuned analysis for all measured samples. The measurement was done three times with a 10 min waiting time between the measurements.

2.5 Thermocalc and Comsol

Thermocalc 2020a (TCFE9.1 steel database, MOBFE5 mobility database) was used to calculate heat-treated matrix compositions and the resulting solidus and liquidus temperatures for differently heat-treated substrates. A heat transfer model of copper mold casting was created in Comsol to estimate the cooling rate of the cast sample. Solidification was modeled with temperature-dependent heat capacity, which was calculated with Thermocalc. Other thermal properties were modeled as constant. Properties for the copper mold were taken from the Comsol library. Thermal conductivity of 27 W/m*K was used for the steel. The initial temperatures for the casting and the mold were 1500 and 23 °C, respectively.

3. Results

3.1 Substrates

The substrates were characterized with SEM, optical microscopy, hardness testing, and XRD. Optical microscopy was used to see the grain morphologies in the substrates and to measure melt pool dimensions. SEM and EBSD were used to determine the phase fractions of ferrite/martensite and residual austenite. In addition, parent austenite grains were reconstructed from the EBSD data with the MATLAB algorithm presented by Nyyssönen et al. (Ref 32). SEM analysis of annealed substrate was not conducted because it should not contain any residual austenite due to slow cooling. XRD was used to qualitatively detect austenite, martensite, and ferrite. Since the XRD peaks of ferrite and martensite overlap, making the characterization difficult, hardness testing was used to differentiate ferritic structure from martensite. Micrographs of the substrates are shown in Fig 2, 3, and 4, and reconstructed parent austenite grains are shown in Fig 5. Hardness and the amount of residual austenite are shown in Fig. 7.

Figure 5 shows the differences in parent austenite grain size. The thermomechanically formed samples shown in 5b and 5d show smaller prior austenite grains than those in 5a and 5c, which were solidified from the melt. The cast sample in 5c shows larger prior austenite grains than the L-PBF sample due to differences in the cooling rate. Figure 6 presents the XRD patterns of the investigated substrates. In every sample the most profound peaks are for ferrite/martensite. The L-PBF sample shows a distinctive peak for residual austenite, whereas in the cast sample, residual austenite is seen as the broadened bottom of the main peak. Q and QT samples show broadened main peaks compared to the annealed sample, indicating the presence of residual stresses, residual austenite, or both.

Annealed (as-delivered) substrate was characterized as soft ferrite with embedded carbides, as shown in Fig 2. According to the steel's datasheet (Ref 33), the hardness in this state should be below 247 HV (235HB), but here the hardness was slightly higher at 260HV, as indicated in Fig 7.

The Q sample has a martensitic microstructure, as shown in Fig 2, and high hardness, as shown in Fig 7. Relatively long etching was needed to reveal the prior austenite grain boundaries, which resulted in the poor visibility of carbides. The less etched sample in Fig 3 reveals a high amount of spherical primary carbides after quenching. The QT microstructure is a fine-grained martensitic structure with a similar visible carbide structure as the Q sample. Retained austenite was not detected in XRD measurements. EBSD analysis showed that the amount of retained austenite in the QT sample is lowest among the investigated samples. Hardness is slightly reduced during tempering, as is expected. Hardness and the amount of residual austenite are shown in Fig 7 as well. The cast substrate consists of large martensite colonies with residual austenite and some carbides at the grain junctions. The average cooling rate according to the Comsol simulation was 61 °C/s. H13 is through-hardenable by air cooling up to 150 mm thickness (Ref 9), leading to a mostly martensitic structure in the copper mold cast as well. A martensitic matrix is also supported by the optical micrograph in Fig 2 and high hardness presented in Fig 7. The L-PBF substrate in Fig 4 shows a very fine-grained microstructure with a substantial amount of finely dispersed residual austenite in a martensitic matrix. A noticeable amount of residual austenite can be seen in the XRD curve as well as in the EBSD analysis. The hardness of L-PBF substrate is the lowest among the martensitic substrates.

Due to the small size of the possible austenite islands, some austenite may have remained undetected. On the contrary, detectable FCC carbides are counted into the residual austenite fraction because the EBSD measurement does not differentiate between chemical compositions. Since carbides larger than a few hundred nanometers should not be present in L-PBF H13 in its manufactured state (Ref 34), this error should be less pronounced in the L-PBF sample compared to the heat-treated and cast samples that have larger carbides. However, the effect of carbides may be minor because similar residual austenite content after tempering has been reported by Pérez and Belzunce after carbide correction (Ref 35).

3.2 Single-Scan Tracks

Figure 8 shows that the hardness in the melt pool is similar regardless of the base material hardness. For cast and Q substrates where the base material hardness is already high, the hardness produced in the single-scan track is only slightly increased. For the soft annealed substrate condition, the scan track is hardened significantly, indicating hardening by carbon dissolving from the primary carbides, leading to a martensitic transformation during cooling. Figure 8 shows the hardness profiles for two different scanning parameters that correspond to high energy input (crosses) and modest energy input (circles). It can be noticed that there is no significant difference in the melt pool hardness regardless of the parameters.

Cracking was not observed for any studied parameter combination when the substrate was in a soft annealed condition. In hardened conditions (Q, QT, cast, L-PBF), cracking was observed when the energy input was too high, namely >0.36 J/mm in this case. With the L-PBF substrate condition, cracking at high energy input was only seen with the highest line energy, even though Fig 8 clearly shows that the hardness of the L-PBF substrate is high and comparable to the hardened substrate conditions. However, small cracks through the melt–solid interface (as shown in Fig 10) were characteristic

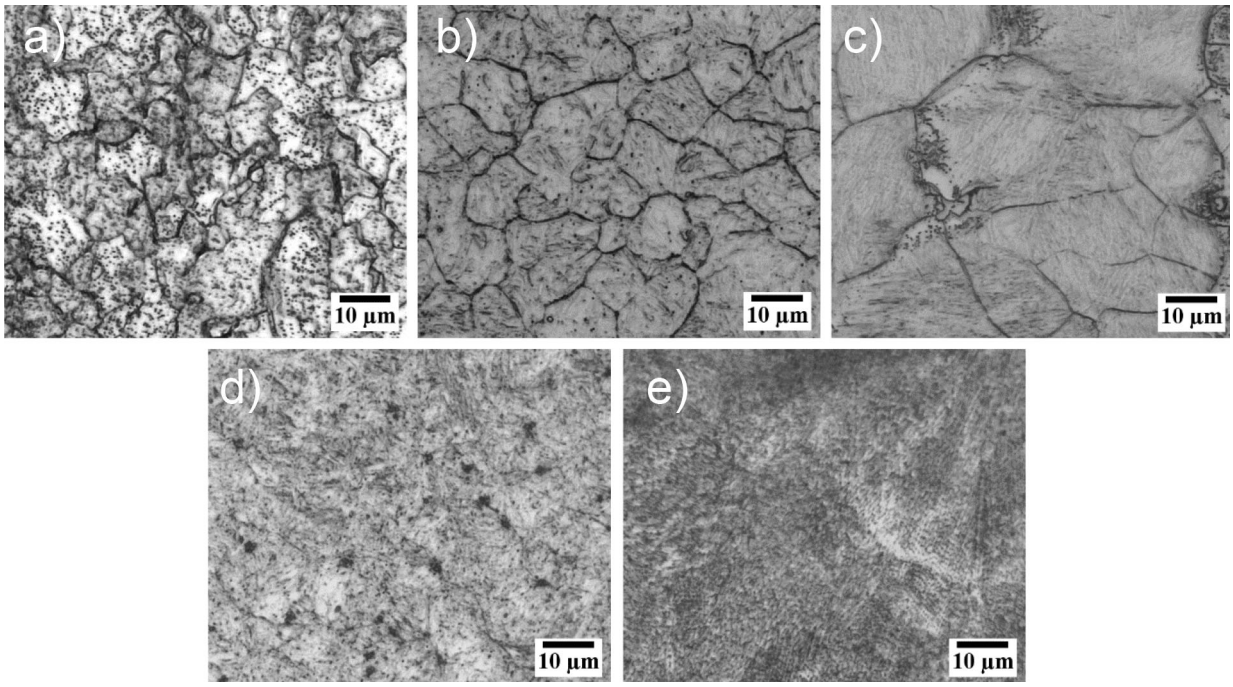

Fig. 2 Optical micrographs of samples that were (a) annealed, (b) oil quenched, (c) copper mold cast, (d) quenched in oil and tempered once, and (e) manufactured with L-PBF

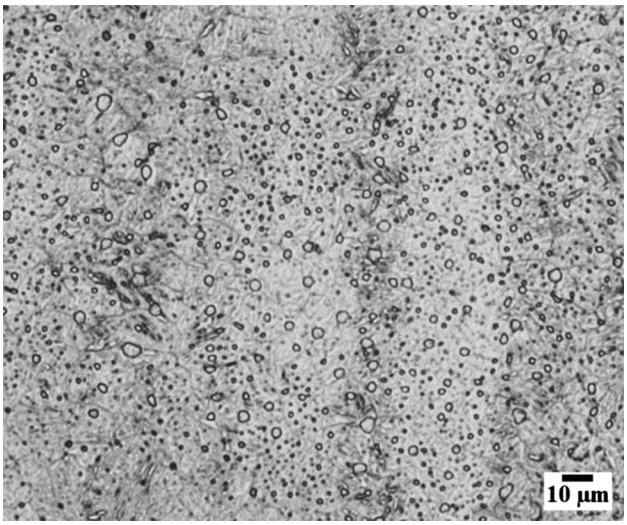

Fig. 3 Oil-quenched sample (the same as in Fig. 2) with a high amount of visible primary carbides. Shorter etching time was used than in Figure 2.

of the cast and L-PBF substrates. The crack type with respect to substrate and parameters is shown in Fig 9 Cracks were categorized by their location either in the melt pool or in the heat affected zone (HAZ), or both (Fig 10).

Single-scan tracks produced with de-focusing parameters (shown in Table 3) did not result in cracking even though high line energy was used. These parameters created comparable or larger melt pool areas compared to the high-energy single-scan tracks that led to cracking. The difference was that with de-focusing, the melt width is increased and the melt depth decreased. Figure 11 further shows the effect of de-focusing on the melt pool geometry. As can be seen, for the same melt cross-sectional area, a larger line energy is needed in the de-focused condition due to reduced energy density, which includes the laser spot size. This is important to note as it shows that one cannot draw the conclusion that increased melt area leads to cracking—rather, the melt pool geometry has to be deep and narrow to induce melt centerline cracking.

From Fig 12, we can see that there is a linear relationship between the line energy and the total melt area when the laser spot size is constant. This shows that a comparison of line energies and drawing a correlation between line energy and a response (such as a cracking tendency) is only relevant if the focus position and laser spot size remain constant. There is also a linear relationship between penetration depth and line energy, whereas melt width increases more rapidly during low heat inputs, corresponding with conduction and transition-mode melting. After the energy input is high enough for severe keyhole-mode processing, the melt width no longer increases as rapidly. It can further be seen that an increased melt area for L-PBF mainly manifests as increased width, not penetration, of the melt.

Figure 13 further shows the melt area for the studied substrate condition. The most rapidly solidified substrate, which is L-PBF, shows roughly 14% larger melt area than the annealed one. Melt pools in the cast and quenched substrates were 8% larger and in the QT sample 3% larger than in annealed sample. It becomes clear that thermal history affects the melting behavior of the material.

The margin of error in melt areas was determined by using a subset of 46 measurements. The set consisted of melt area measurements for 23 duplicated parameter–substrate combinations. Relative difference ($|A_1-A_2|/((A_1+A_2)/2)$) was calculated for each parameter-substrate combination. Resulted 23 relative differences were averaged to form the average error of 5.6%.

All the measurements that were used to calculate the average melt areas are shown in Table 4

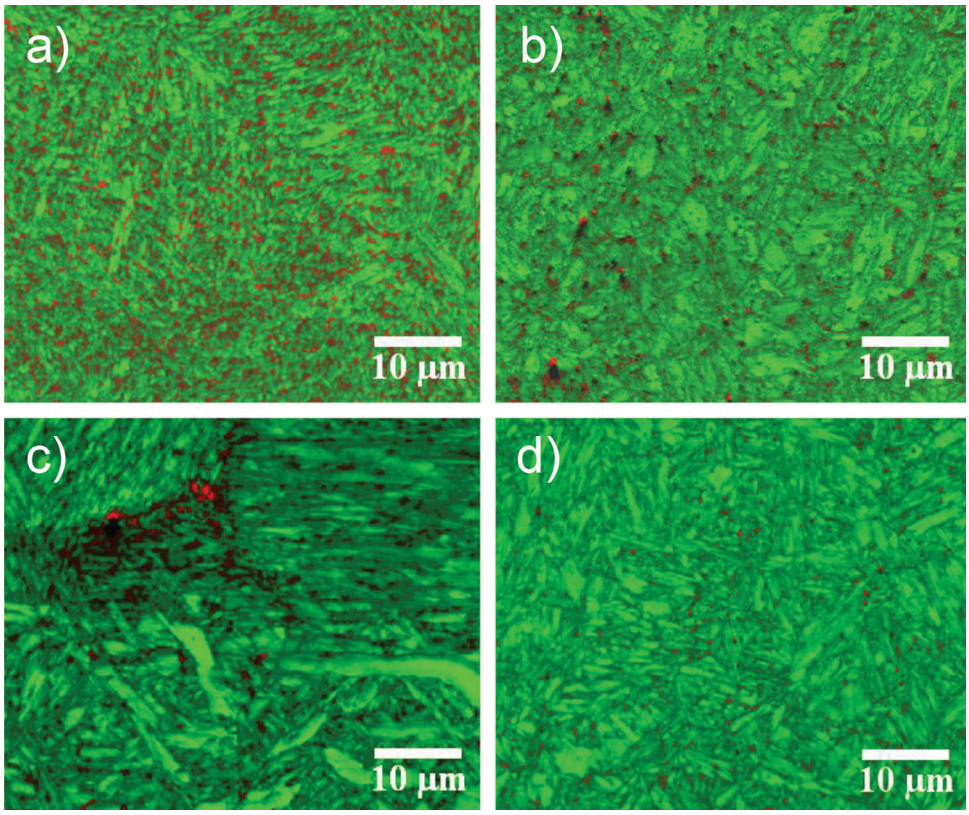

Fig. 4 EBSD images of the tested samples. The green phase is body-centered cubic (BCC), and the red phase is face-centered cubic (FCC). The sample treatments are (a) L-PBF, (b) oil quenched, (c) copper mold cast, (d) oil quenched and tempered once.

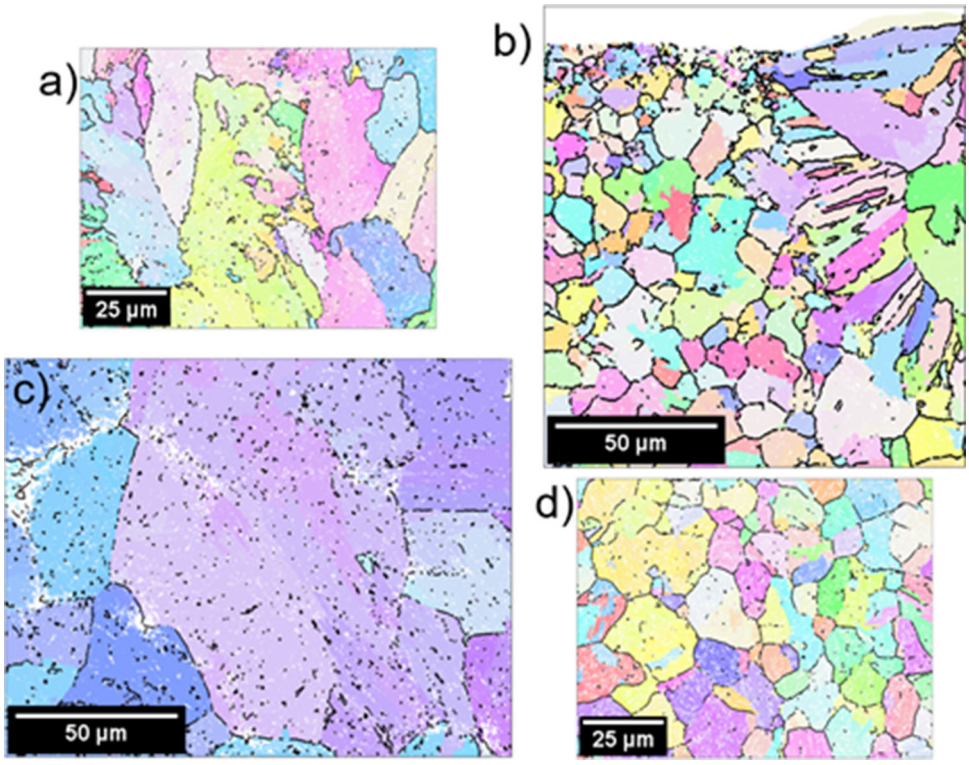

Fig. 5 Reconstructed parent austenite grains in the tested substrates. The sample treatments are (a) L-PBF, (b) oil quenched, (c) copper mold cast, (d) oil quenched and tempered once. The images are resized to be shown at the same scale. One half of a single track is visible in the upper right corner of 5b.

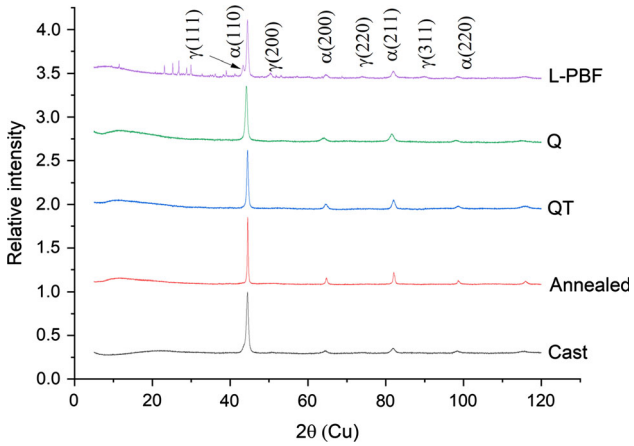

Fig. 6 XRD patterns of the sample substrates. The XRD curve for the L-PBF sample has some noise originating from the sample mounting.

From Table 4, we see that with low line energies the substrate resulting in largest melt area is ambiguous. When line energy is above 0.2 L-PBF, cast and Q substrates show the largest melt pools. The clearest difference can be seen between L-PBF and annealed substrates. The microstructure in the melt pool was not seen to differ between substrates, although the characterization was mainly done with optical microscopy.

3.3 Computational Thermodynamics

Thermocalc software was used to estimate the effect of metastable composition on the melting point and hence on melting behavior of differently heat-treated substrates. Liquidus and solidus temperatures were calculated for each substrate based on its matrix' composition. Matrix composition represents the composition of the dominating body centered cubic (BCC) phase from which elements have escaped into carbides or they have remained in a supersaturated solution. A phase fraction–temperature diagram of W302 (H13) was calculated as

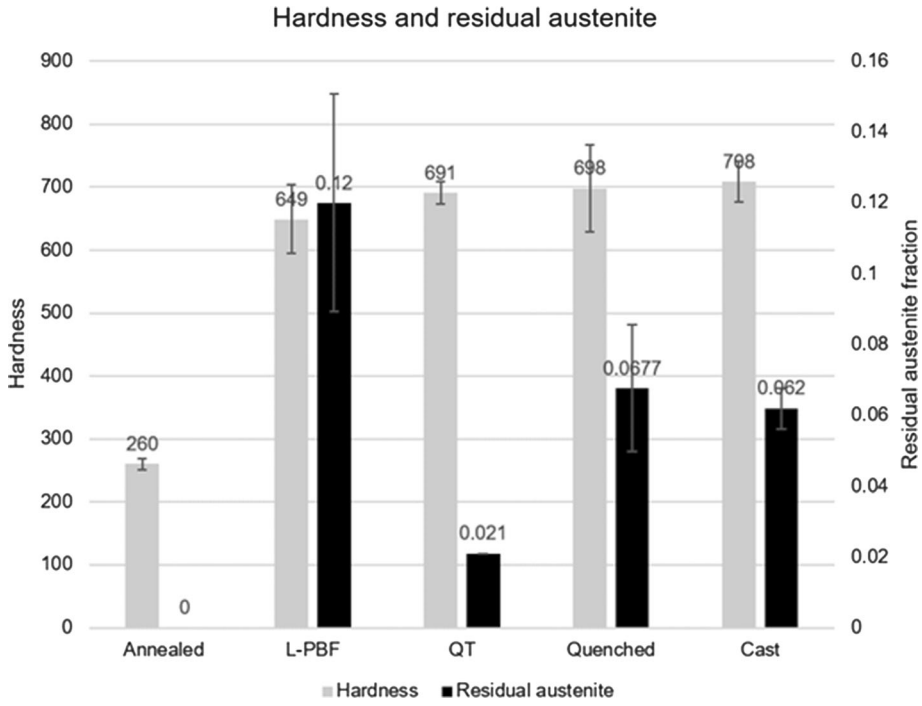

Fig. 7 Substrate hardness (HV0.1) and the residual austenite (EBSD) volume fraction. The annealed sample was not analyzed with EBSD, and the QT sample was analyzed only once. For others, residual austenite was measured from multiple images and averaged.

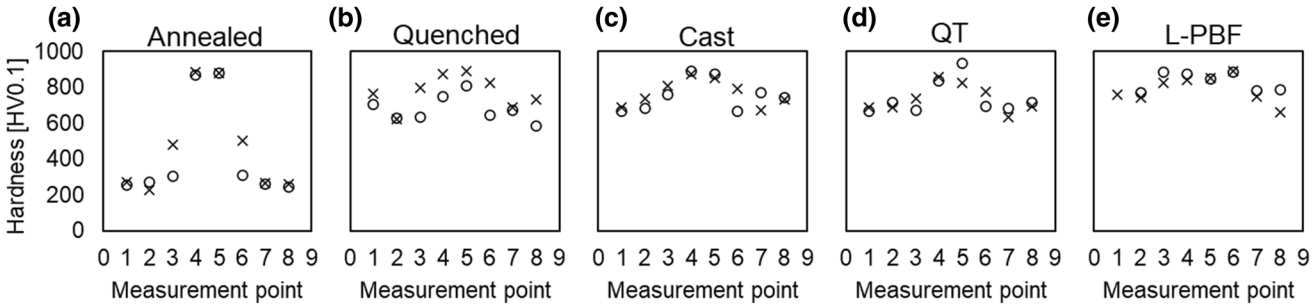

Fig. 8 Hardness profiles (HV0.1) over the single-track scans for the studied substrate conditions with high energy input (crosses) and modest energy input (circles). Measurement points 4 and 5 are in the melt pool.

No crack
Crack in HAZ
Crack in meltpool
HAZ and meltpool
Line energy (J/mm)
shown in cells

Cast	Scan speed mm/s				
Laser power (W)	500	600	700	800	900
100	0.20	0.17	0.14	0.13	0.11
175	0.35	0.29	0.25	0.22	0.19
250	0.50	0.42	0.36	0.31	0.28
325	0.65	0.54	0.46	0.41	0.36
400	0.80	0.67	0.57	0.50	0.44

Quenched	Scan speed mm/s				
Laser power (W)	500	600	700	800	900
100	0.20	0.17	0.14	0.13	0.11
175	0.35	0.29	0.25	0.22	0.19
250	0.50	0.42	0.36	0.31	0.28
325	0.65	0.54	0.46	0.41	0.36
400	0.80	0.67	0.57	0.50	0.44

L-PBF	Scan speed mm/s				
Laser power (W)	500	600	700	800	900
100	0.20	0.17	0.14	0.13	0.11
175	0.35	0.29	0.25	0.22	0.19
250	0.50	0.42	0.36	0.31	0.28
325	0.65	0.54	0.46	0.41	0.36
400	0.80	0.67	0.57	0.50	0.44

Quenched and tempered	Scan speed mm/s				
Laser power (W)	500	600	700	800	900
100	0.20	0.17	0.14	0.13	0.11
175	0.35	0.29	0.25	0.22	0.19
250	0.50	0.42	0.36	0.31	0.28
325	0.65	0.54	0.46	0.41	0.36
400	0.80	0.67	0.57	0.50	0.44

Annealed	Scan speed mm/s				
Laser power (W)	500	600	700	800	900
100	0.20	0.17	0.14	0.13	0.11
175	0.35	0.29	0.25	0.22	0.19
250	0.50	0.42	0.36	0.31	0.28
325	0.65	0.54	0.46	0.41	0.36
400	0.80	0.67	0.57	0.50	0.44

Fig. 9 Cracks resulting from each substrate–parameter combination

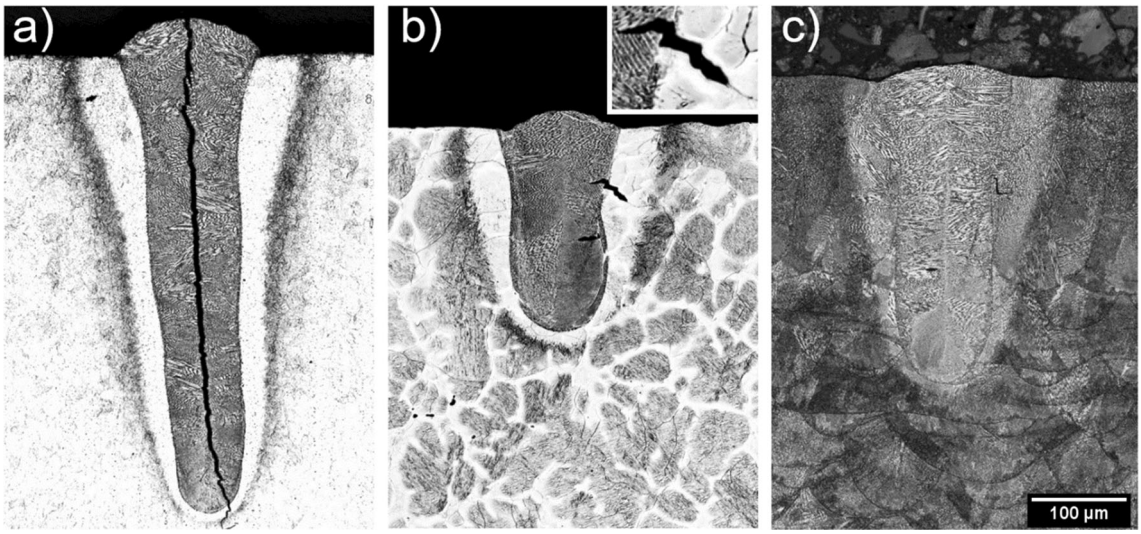

Fig. 10 Two different crack types observed in the single-track cross sections: (a) a vertical crack at the melt centerline, (b-c) horizontal cracks propagating from HAZ to melt over the fusion line

Table 3 Parameters for de-focused single-track lines

	Scan speed, mm/s	Power, W	Line energy, J/mm	Change in focal length, mm
De-focus 1	700	400	0.57	-4
De-focus 2	700	400	0.57	-6
De-focus 3	500	400	0.8	-4
De-focus 4	500	400	0.8	-6

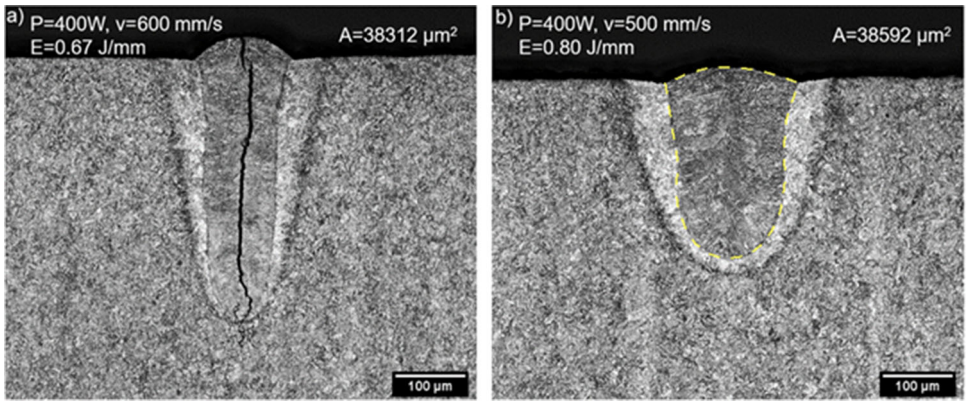

Fig. 11 Melt pools with approximately the same melt area. The cracking here is shape dependent. Measured area is shown on the right with a dashed yellow line.

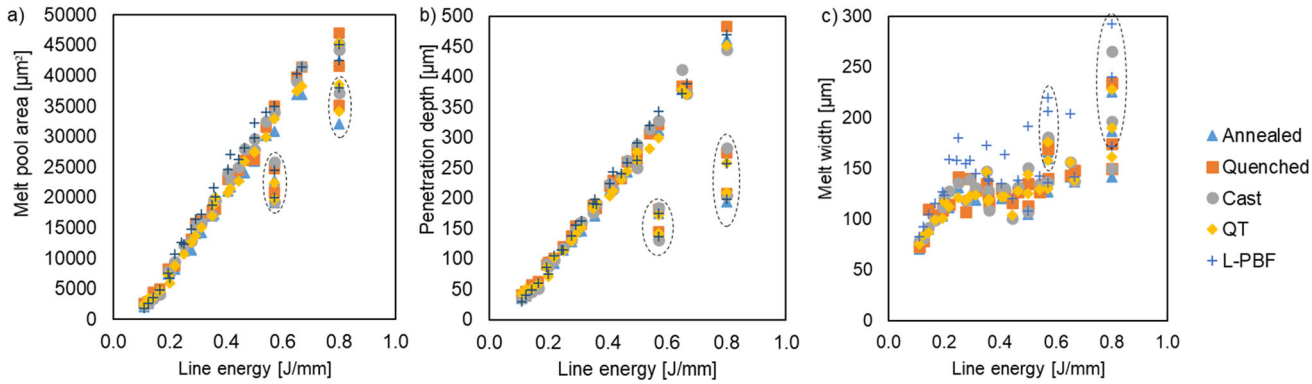

Fig. 12 Melt pool dimensions for each studied substrate condition: (a) the total cross-sectional area, (b) melt penetration, and (c) melt width. Dashed circles indicate the results of de-focused samples.

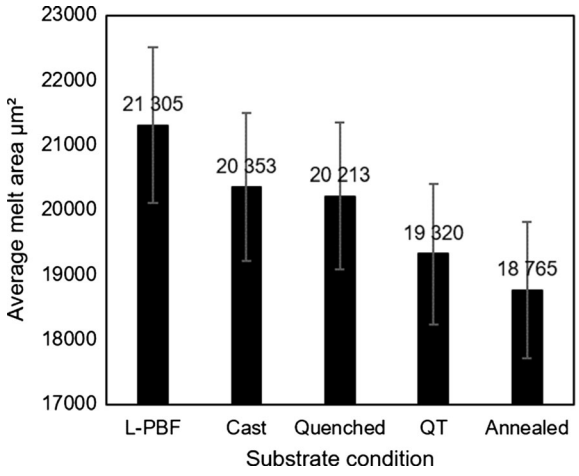

Fig. 13 Average melt area for all the studied parameters and substrate conditions. Melt pool area is the average of 24 different power–speed combinations

a starting point and is shown in Fig 14. Figure 14 shows a ferrite-austenite transformation taking place at around 850 ºC and stable primary carbides below 1120 ºC. These transformations are connected to the matrix composition, because below 850 ºC alloying elements are transferred from BCC matrix into carbides. When the temperature is above 1120 ºC, all carbides are dissolved and matrix composition is the same as the nominal composition. According to the datasheet of W302, the material is delivered in annealed condition (Ref 33). Annealing consists of holding at 750-800 °C, followed by slow cooling at 10-20 °C/h, till it cools down to 600 °C, followed by cooling in air. Since the cooling is slow, the as-delivered phase structure and BCC matrix composition are assumed to be a near the equilibrium phase structure that was present at 600 °C. Similarly, the matrix composition of the Q sample is assumed to represent the equilibrium composition at 1080 °C. The effect of tempering was taken into account by inserting the Q matrix composition into the Thermocalc Precipitation module. The precipitation matrix was set to BCC. Nucleation calculations were done for carbide types M6C, M5C2, M7C3, M3C2, and M23C6 in order to see which one precipitates during tempering. M23C6 is the equilibrium carbide, but because of the rapid cooling and low tempering temperature, M23C6 does not form—instead, the metastable M7C3 carbide is kinetically selected. Calculations showed M7C3 carbide to precipitate first, which is in accordance with the reaction sequence shown by Inoue and Masumoto (Ref 36) where M7C3 precipitates before M23C6 by transforming from cementite. It is also mentioned in (Ref 5) that Cr7C3 carbides precipitate in chromium-containing steels when the tempering temperature is 500 °C. Therefore, nucleating carbide was assumed to be M7C3, even though the presence of MC and M23C6 type secondary carbides has been reported (Ref 37, 38). The interfacial energy between M7C3 and BCC matrix was calibrated according to (Ref 38) to result

Table 4 Scan parameters and resulting melt area (μm^2) in each substrate. Grayscale formatting indicates the relative size of the melt pool between substrates scanned with the same parameters.

Laser parameters			Substrate condition and melt area (μm²)				
Line energy (J/mm)	Speed (mm/s)	Power (W)	L-PBF	Cast	Q	QT	Annealed
0.11	900	100	1830	2356	2634	2566	2066
0.13	800	100	2676	2675	2940	3414	2656
0.14	700	100	3587	3404	4457	3664	4021
0.17	600	100	4776	4088	4957	4681	4581
0.19	900	175	7593	7827	8292	7224	7441
0.20	500	100	6788	7740	8013	5896	8060
0.22	800	175	10730	9430	8774	8821	8182
0.25*	700*	175*	12328	12210	-	10760	11183
0.28	900	250	14796	12891	13141	12575	11434
0.29	600	175	16426	15421	15702	13674	14121
0.31	800	250	17325	15910	16135	15132	14249
0.35	500	175	18784	17104	17800	17003	16963
0.36	700	250	21574	19676	18433	18917	17264
0.36	900	325	20082	19607	18054	20050	18435
0.41	800	325	24615	24036	23022	20750	21072
0.42	600	250	27116	22910	23456	21521	21730
0.44	900	400	26323	25082	24505	22666	23383
0.46	700	325	28194	28099	26188	25969	24054
0.50	500	250	29845	29722	27302	27511	26008
0.50	800	400	32282	27910	26294	27491	27719
0.54	600	325	34115	32560	31646	29939	30270
0.57	700	400	35073	34033	35072	32998	30895
0.65	500	325	40324	39091	39734	37497	36912
0.67	600	400	41425	41621	41489	38312	36974
0.80	500	400	45045	45287	47065	45418	41858
Average melt area			21305	20353	20213	19320	18765

*row not included to average due to missing data.
Margin of error in single measurements is ± 5.6%

in similar total carbide content with the same thermal history. Because tempering takes place at constant temperature, a constant interfacial energy of 0.5 J/m^2 was then used for the precipitation simulation.

The matrix composition of the cast substrate was evaluated with a two-step method. First, a Scheil solidification calculation with back diffusion was conducted with Thermocalc using the nominal composition of W302. Solidification was assumed to be completed at 11.5% liquid, which represents the amount of the grain boundary phase shown in Fig 15. This is higher than the amount of residual austenite (6.2%) shown in Fig 7 because the last liquid decomposes into austenite and carbides. The high carbon grain boundary austenite present at a high temperature may undergo further phase transformations upon cooling, leading to the final low temperature residual austenite shown in Fig 4.

The solidified matrix composition was then inserted in the precipitation module with the same 61°C cooling rate. The volume fraction of nucleated M7C3 in the cast sample was negligible, so the composition from a Scheil simulation was used. It should be noted that calculations done with the precipitation module are subject to significant uncertainties regarding precipitation parameters, such as carbide–matrix interfacial energy and dislocation density.

The L-PBF substrate was approximated as a supersaturated solid solution with the nominal composition, for which the equilibrium values for liquidus and solidus temperatures were

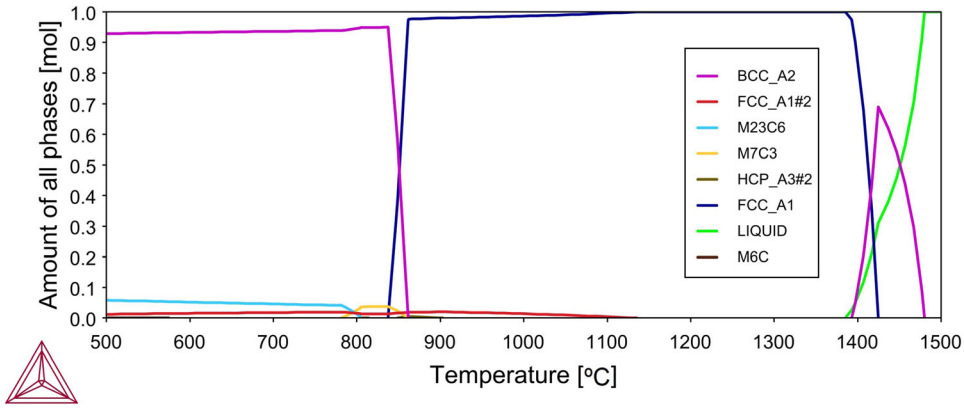

Fig. 14 Equilibrium phase fraction vs. temperature graph for W302

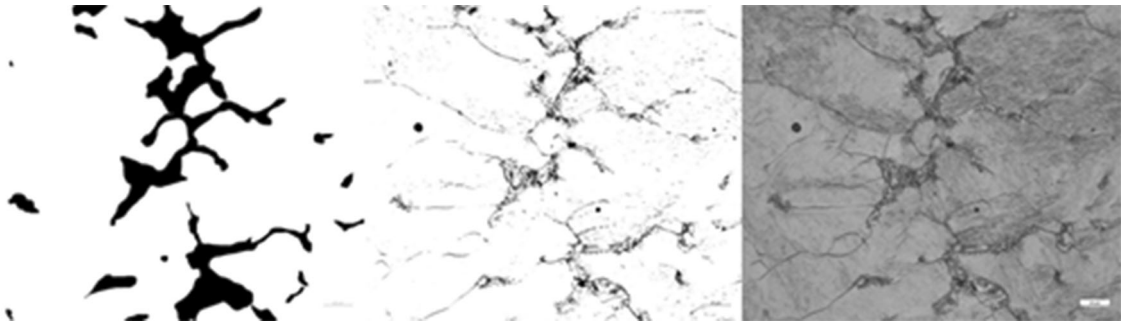

Fig. 15 Cast sample grain boundary phase (dark parts or mixed white + dark parts). Measurement showed 11.5% of the grain boundary phase, which consists of at least residual austenite and carbides. Two micrographs were used for volume fraction measurements.

used. The results for solidus and liquidus temperatures with respect to the heat treatment state are shown in Table 5.

As shown in Table 5, significant differences exist between matrix solidus and liquidus temperatures where the greatest difference of over 130 °C is between the annealed and L-PBF substrate solidus. These calculations suggest that it is much easier to locally melt quenched than annealed material.

Figure 16 shows the correlation between single-track melt area and substrate solidus temperature when scan speed is kept constant at 700 mm/s. Power of 100 W shows no correlation with R^2 value of only 0.07, but powers of 175, 250, 325, and 400 W show R^2 values of 0.19, 0.61, 0.68, and 0.82, respectively.

3.4 Thermal Conductivity

To assess the effect of thermal conductivity of the substrate on the resulting melt area, thermal conductivities were measured and are shown in Table 6. Same parameter sets as in chapter 3.3 were selected for correlation analysis in Fig 17. It can be seen that with low power the R^2 value between melt area and substrate thermal conductivity is poor showing no correlation. The R^2 value increases with power and peaks at 0.96 when the power was 400 W.

4. Discussion

This study demonstrated that thermal history affects the material's melting behavior under rapid heating as well as the resulting crack type. Melt area was found inversely proportional to the investigated thermal properties, thermal conductivity, and solidus temperature, as shown in Fig 16 and 17. Both measures showed decent R^2 correlation with melt area when heat input was sufficiently high, but the effect of thermal conductivity on melt area seems larger than the effect of solidus. Considering mechanical properties, substrate and melt pool hardness were examined as shown in Fig 8. All substrates showed similar hardness profile over the scanned line except the annealed substrate, which was considerably softer than the others. Hardness of the rapidly solidified single track was similar in all conditions. Microstructural features such as present phases, amount of residual austenite, and size of parent austenite grains were characterized to explain the cracking behavior. Based on the micrographs, the cast substrate showed most similar cracking mechanism when compared to the L-PBF substrate. This presumably originates from the solidification where parent austenite grain remains larger than in thermomechanical processing. Overall, the results emphasize the importance of substrate selection when evaluating materials printability with single-track scan method because cracking type appears to be substrate dependent. Additionally, AM process parameters such as suitable layer thickness and hatch distance for a given scan speed and power combination can be predicted more accurately when the formed melt pool geometry is representative of the rapidly solidified AM material.

When the material solidifies rapidly from the melt (the L-PBF sample), the matrix composition remains close to high temperature equilibrium composition, meaning its solidus and liquidus temperatures are close to equilibrium values. When annealing below solidus (annealed, Q, QT samples), more stable phases, such as carbides, can be formed from the

Table 5 Calculated liquidus and solidus temperatures of the matrix for different heat treatment states

Heat treatment	Calculated matrix composition, wt.%								
	Fe	Cr	Si	Mn	Mo	V	C	T_Sol.	T_Liq.
L-PBF (H13 OES)	90.41	5.18	1.02	0.38	1.50	1.11	0.40	1376.58	1478.25
Quenched	91.18	5.10	1.00	0.40	1.27	0.72	0.33	1407.72	1486.23
QT	91.25	5.06	1.00	0.40	1.26	0.70	0.32	1409.88	1487.23
Cast	91.64	4.92	0.98	0.37	1.13	0.76	0.20	1421.07	1498.19
Annealed	95.19	2.75	1.06	0.42	0.38	0.20	0.00	1513.39	1519.4

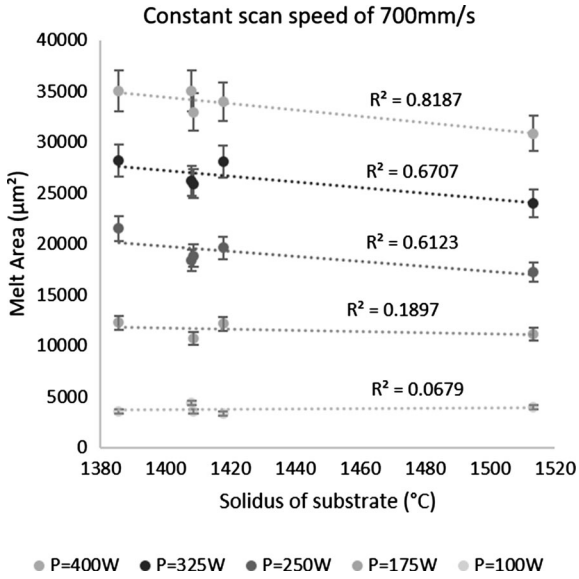

Fig. 16 Melt area as a function of substrate solidus temperature for constant scan speed of 700mm/s

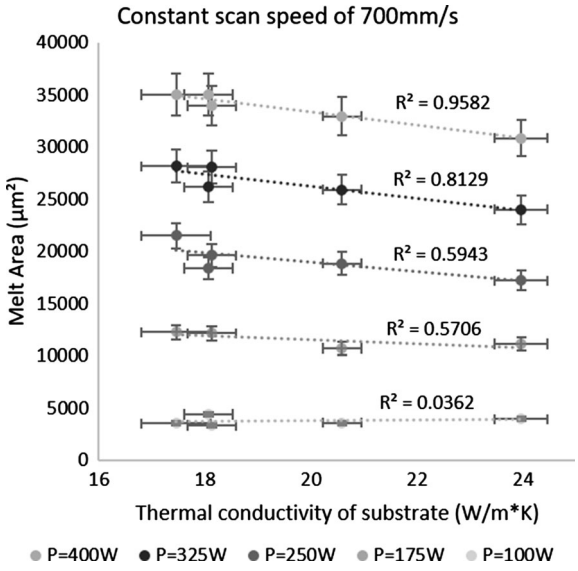

Fig. 17 Melt area as a function of substrate thermal conductivity with constant scanning speed of 700mm/s

Table 6 Thermal conductivities of tested substrates

1s 400mW average of 3 measurements	Thermal conductivity W/m*K	Standard deviation
Annealed	23.97	0.50
Q	18.07	0.46
Cast	18.13	0.46
QT	20.59	0.36
L-PBF	17.46	0.66

supersaturated solution. The stable fraction of carbides increases when lowering the annealing temperature, as shown in Fig 14. These carbides deplete the matrix of carbon, vanadium, chromium, and other carbide-forming elements, altering the matrix composition and, hence, increasing the matrix solidus temperature as shown in Table 5. When heated rapidly, which is the case in L-PBF, there is no time for diffusional homogenization prior to melting, allowing the alloy matrix to have different solidus depending on the thermal history. In addition to carbides, residual austenite can alter the matrix composition. The size of the melt pools seems to follow the amount of residual austenite. This is in accordance with the work of Shingu and Ishihara (Ref 29) and shows the easiest melting of the least stable microstructure. However, the R^2 values in Fig 16 for substrate solidus and melt area show lower values than for correlation between thermal conductivity and melt area.

Here the difference in melt pool area between the Q and QT samples cannot be explained by the solidus temperature, but it can be explained by a difference in thermal conductivity. It has been shown that tempering increases steel's thermal conductivity significantly when compared to a Q state (Ref 39), which is in accordance with the present measurements. A numerical investigation about the effects of thermal conductivity and melting point on melt pool dimensions in electron beam melting has been made by Cheng and Chou. They show melting point being the main factor affecting melt pool size when thermal conductivity is kept reasonably similar, which was the case within Ti64, In718, 316L, and TiAlNb calculations. With copper, they found high thermal conductivity

exceeding the effect of melting point. (Ref 40) The thermal conductivity of H13 is quite low varying between 17.46 and 23.97 W/m*K, but since the melting points of the Q and QT matrices are practically the same and the effect of other thermal properties (such as specific heat) is found to have a minimal effect (Ref 41), the resulting difference in melt pool size can be deduced to originate from different thermal conductivities. Therefore, based on the R^2 correlation values and difference between Q and QT melt areas, thermal conductivity shows a greater effect on melt pool size than the substrate melting point. The effect of thermal conductivity, however, is not clear with low heat input values. This is considered to originate from the competitive heat transfer between surface radiation plus convection and conduction within the material. Laser spot size determines the radiative area from the surface, whereas heat input and keyhole formation affects the melt boundary area below the surface. Low heat input results in small penetration, increasing the proportion of radiative and convective heat loss from the surface. Therefore, the effect of thermal conductivity on melt pool size is reduced with low heat input.

Melt area was not a sufficient measure to estimate the cracking tendency. The L-PBF substrate had the largest melt pools, but only very small cracks were observed in the cross-sections. The Q sample had smaller melt pools than the L-PBF sample, but it cracked more often and more severely than the L-PBF sample. The QT sample had smaller melt pools and less cracks than the Q sample, but it still cracked more than the L-PBF substrate. It seems that the amount of residual austenite does not solely explain cracking tendency either, because the QT sample had the least residual austenite but still had reasonable tolerance for cracking.

Figure 10 shows the two different types of crack observed. Figure 10a shows a vertical crack along the melt centerline. This type of cracking is only observed at high-energy input and when the resulting melt pool geometry is deep and narrow. Such melt geometry is known to promote weld centerline cracking (Ref 42). These types of cracks were only observed in the hardened substrate states (the Q, QT, cast states) but, not in the L-PBF substrate that ha similar hardness. Centerline cracks could be due to a higher impurity content in the W302 feedstock (the annealed, Q, QT, cast substrates) than in the H13 powder supplied by SLM Solutions (the L-PBF substrate). Even though the nominal composition was the same, a slightly higher sulfur and phosphorus content in W302, combined with the high heat input, resulting in a slower cooling rate and extending the time for impurity segregation into the last liquid portion, could cause such cracks. Copper content is also higher in W302 than in SLM Solutions' H13, but its effect is usually restricted to HAZ rather than centerline cracking (Ref 43).

The other type of crack observed are the horizontal cracks propagating from HAZ to the melt over the fusion line. These cracks were only observed in the cast substrate (Fig 10b) and L-PBF substrate (Fig 10c) conditions. According to Lippold (Ref 42), cracking in HAZ can be so-called *reheat cracking*. Reheat cracking is associated with a coarse grain zone in the HAZ, carbide dissolution, and precipitation due to thermal cycling, residual stresses in the weld, and substrate and stress relaxation during heating. Fulfilment of these requirements varies between substrates. In the cast sample, Fig 10(b) shows that the crack has propagated through the prior austenite grain boundary. The cooling rate in the cast sample was relatively slow, leading to the large prior austenite grains and carbides at the grain boundaries shown in Fig 4. Simultaneous strengthening of the grains and embrittlement of grain boundaries by carbide nucleation results in the grain boundary being the weakest point. Additionally, there are residual stresses in the sample from the casting procedure because the sample was not stress relieved prior to single-track testing. The reheat crack in the HAZ of the cast substrate forms when the resultant residual stresses (the combined effect of forming and existing stresses) relax after solidification. The role of large prior austenite grains is valid for the L-PBF substrate as well since their size is comparable to the cast sample, as is shown in Fig 5. As opposed to the cast sample, carbides have not been reported in as manufactured H13 (Ref 34, 44), but the thermal cycle at the single-track HAZ could be sufficient to nucleate them at grain boundaries. Work by Åsberg et al. (Ref 45) on heat-treated L-PBF H13 shows there is a continuous network of carbides along the few-micron-sized prior austenite grain boundaries after prolonged stress relieving at 650 °C. Such a structure could perhaps form in the HAZ very close to the melt boundary because the temperature is much higher than 650 °C and because fine grain size enhances grain boundary diffusion, which is four to six orders of magnitude higher than diffusion inside the grain (Ref 46). This kind of continuous carbide structure combined with large prior austenite grains can be brittle regardless of the small martensite grain size and could explain the reheat cracking tendency of the L-PBF sample in the vicinity of the melt pool. Further characterization might show the crack propagating in the carbide network at the prior austenite grain boundary, very close to the melt pool. Possible reason why this kind of carbide network has not been found in bulk manufactured H13 samples is because the single-track HAZ structure is destroyed by the following layers. As shown in Fig 10, the HAZ shrinks when going deeper into the melt pool. Because each layer has to be fused onto the substrate, the bulk samples mostly consist of the lower parts of the melt pools where the HAZ is a lot smaller or does not even exist, as in Fig 10(a). Reheat cracking was not observed in the Q or QT samples. The prior austenite grain size is quite small in the Q and QT samples because they were not solidified from melt but quenched at a temperature designed to avoid excessive austenite grain growth. At the quenching temperature, a small amount of primary carbides should already be present, as shown in Fig. 14. The existence of primary carbides would lower the driving force for secondary carbide formation since the matrix composition is already depleted of carbide-forming elements. Therefore, the formation of carbides in the grain boundaries of HAZ is less likely in quenched substrates than in solidified substrates, showing in the Q and QT substrates being more tolerant of reheat cracking. Therefore, such a crack type was only seen in the L-PBF and cast samples.

5. Conclusions

Single-track tests revealed the heat treatment state of the substrate to have an effect on the melt pool size and cracking type. Deep melt pools can cause cracks in the center of the melt pool, where the final melt is situated, alluding to a segregation-based phenomenon. Small horizontal cracks in the heat-affected zone propagate along prior austenite grain boundaries, indicating grain boundary embrittlement in the heat-affected zone.

Thermal history has an effect on alloying element distribution, affecting the matrix composition and thus the melting

point under rapid heating. Similarly, the thermal conductivity of the substrate varies based on the thermal history. Both solidus temperature and thermal conductivity are inversely proportional to the cooling rate of the H13 substrate. Due to better R^2 correlation between thermal conductivity and melt pool area, and the difference between Q and QT samples, thermal conductivity is considered to have the larger role over substrate solidus on the melt pool size.

Since hot cracking, segregation, and other metallurgical phenomena require no powder to take place, it is suggested that an alloy's printability regarding metallurgical and microstructural issues can be evaluated without introducing powder to the process if the substrate condition is chosen carefully to represent that of a rapidly solidified material. Quenching a substrate from a sub-solidus temperature or using an annealed substrate may result in fallacious matrix composition and microstructure, resulting in non-representative thermal conductivity and hence inaccurate melt pool sizes and wrong cracking mode. The cast sample was the only one showing similar cracking as in the L-PBF substrate due to the similar parent austenite grain size in these two samples. Therefore, if a material's printability is to be estimated with single-track scanning, a rapidly solidified substrate should be preferred rather than a quenched one.

Naturally, defects that are partially dependent on powder properties—such as a lack of fusion, melt-track balling, or poor wetting—cannot be evaluated without powder. Separate measures are also needed to evaluate a material's tendency to form and behave under residual stresses.

Acknowledgments

The authors would like to express their gratitude to Mrs. Seija Kivi for the preparation and imaging of the metallographic specimens, to Kimmo Ruusuvuori for operation of the SLM 125 HL system, and to Jarkko Metsäjoki for EBSD measurements. The financial support of VTT Technical Research Centre of Finland is gratefully acknowledged.

Funding

Open Access funding provided by Technical Research Centre of Finland (VTT).

Open Access

Data availability

The raw/processed data required to reproduce these findings cannot be shared at this time due to technical or time limitations, but can be provided upon request.

References

1. EOS GmbH, EOS Materials Metal Portfolio Overview, (2019)
2. SLM Solutions Group AG, Metal Powder Optimised for Selective Laser Melting, (n.d.) 16
3. Renishaw plc, Maraging Steel M300 Powder for Additive Manufacturing * H-5800-3695-01-A *, (2017)
4. Renishaw, SS 316L-0407 Powder for Additive Manufacturing, (2018)
5. H. Bhadeshia and R. Honeycombe, *Temp. Martensite*, 2017 https://doi.org/10.1016/b978-0-08-100270-4.00009-3
6. Y. Bai, Y. Yang, Z. Xiao and D. Wang, Selective Laser Melting of Maraging Steel: Mechanical Properties Development and its Application in Mold, *Rapid Prototyp. J.*, 2018, **24**, pp 623–629. https://doi.org/10.1108/RPJ-05-2017-0104
7. K. Kempen, B. Vrancken, S. Buls, L. Thijs, J. Van Humbeeck and J.-P. Kruth, Selective Laser Melting of Crack-Free High Density M2 High Speed Steel Parts by Baseplate Preheating, *J. Manuf. Sci. Eng.*, 2014, **136**, 061026. https://doi.org/10.1115/1.4028513
8. R. Mertens, B. Vrancken, N. Holmstock, Y. Kinds, J.-P. Kruth and J. Van Humbeeck, Influence of Powder Bed Preheating on Microstructure and Mechanical Properties of H13 Tool Steel SLM Parts, *Phys. Procedia.*, 2016, **83**, p 882–890. https://doi.org/10.1016/J.PHPRO.2016.08.092
9. J.R. Davis, Tool Steels, *ASM Met. Handb.*, 1998 https://doi.org/10.1007/BF00658497
10. R. Cottam, J. Wang and V. Luzin, Characterization of Microstructure and Residual Stress in a 3D H13 Tool Steel Component Produced by Additive Manufacturing, *J. Mater. Res.*, 2014, **29**, p 1978–1986. https://doi.org/10.1557/jmr.2014.190
11. M. Ackermann, J. Šafka, L. Voleský, J. Bobek and J.R. Kondapally, Impact Testing of H13 Tool Steel Processed with Use of Selective Laser Melting Technology, *Mater. Sci. Forum.*, 2018, **919**, p 43–51. https://doi.org/10.4028/www.scientific.net/msf.919.43
12. C.J. Chen, K. Yan, L. Qin, M. Zhang, X. Wang, T. Zou and Z. Hu, Effect of Heat Treatment on Microstructure and Mechanical Properties of Laser Additively Manufactured AISI H13 Tool Steel, *J. Mater. Eng. Perform.*, 2017, **26**, p 5577–5589. https://doi.org/10.1007/s11665-017-2992-0
13. P. Laakso, T. Riipinen, A. Laukkanen, T. Andersson, A. Jokinen, A. Revuelta and K. Ruusuvuori, Optimization and Simulation of SLM Process for High Density H13 Tool Steel Parts, *Phys. Procedia.*, 2016, **83**, p 26–35. https://doi.org/10.1016/J.PHPRO.2016.08.004
14. F. Deirmina, N. Peghini, B. AlMangour, D. Grzesiak and M. Pellizzari, Heat Treatment and Properties of a Hot Work Tool Steel Fabricated by Additive Manufacturing, *Mater. Sci. Eng. A.*, 2019, **753**, p 109–121. https://doi.org/10.1016/J.MSEA.2019.03.027
15. D. Cromier, O. Harrysson, H. West, Characterization of H13 Steel Produced Via Electron Beam Melting, *Rapid Prototyp. J.*, 2004, **10**(1), p 35–41. https://doi.org/10.1108/13552540410512516
16. M. Wang, W. Li, Y. Wu, S. Li, C. Cai, S. Wen, Q. Wei, Y. Shi, F. Ye and Z. Chen, High-Temperature Properties and Microstructural Stability of the AISI H13 Hot-Work Tool Steel Processed by Selective Laser Melting, *Metall. Mater Trans. B Process Metall. Mater Process. Sci.*, 2019, **50**, p 531–542. https://doi.org/10.1007/s11663-018-1442-1
17. J.D. Roehling, A. Perron, J.L. Fattebert, T. Haxhimali, G. Guss, T.T. Li, D. Bober, A.W. Stokes, A.J. Clarke, P.E.A. Turchi, M.J. Matthews and J.T. McKeown, Rapid Solidification in Bulk Ti-Nb Alloys by Single-Track Laser Melting, *Jom.*, 2018, **70**, p 1589–1597. https://doi.org/10.1007/s11837-018-2920-2
18. Y. Guo, L. Jia, B. Kong, N. Wang and H. Zhang, Single Track and Single Layer Formation in Selective Laser Melting of Niobium Solid Solution Alloy, *Chinese J. Aeronaut.*, 2018, **31**, p 860–866. https://doi.org/10.1016/J.CJA.2017.08.019

19. I. Yadroitsev, P. Krakhmalev, I. Yadroitsava, S. Johansson and I. Smurov, Energy Input Effect on Morphology and Microstructure of Selective Laser Melting Single Track from Metallic Powder, *J. Mater. Process. Technol.*, 2013, **213**, p 606–613. https://doi.org/10.1016/J.JMATPROTEC.2012.11.014
20. I. Yadroitsev, A. Gusarov, I. Yadroitsava and I. Smurov, Single Track Formation in Selective Laser Melting of Metal Powders, *J. Mater. Process. Technol.*, 2010, **210**, p 1624–1631. https://doi.org/10.1016/J.JMATPROTEC.2010.05.010
21. S. Lee, J. Peng, D. Shin and Y.S. Choi, Data Analytics Approach for Melt-Pool Geometries in Metal Additive Manufacturing, *Sci. Technol. Adv. Mater.*, 2019 https://doi.org/10.1080/14686996.2019.1671140
22. S. Ghosh, L. Ma, L.E. Levine, R.E. Ricker, M.R. Stoudt, J.C. Heigel and J.E. Guyer, Single-Track Melt-Pool Measurements and Microstructures in Inconel 625, *Jom.*, 2018, **70**, p 1011–1016. https://doi.org/10.1007/s11837-018-2771-x
23. N.T. Aboulkhair, I. Maskery, C. Tuck, I. Ashcroft and N.M. Everitt, On the Formation of AlSi10Mg Single Tracks and Layers in Selective Laser Melting: Microstructure and Nano-Mechanical Properties, *J. Mater. Process. Technol.*, 2016 https://doi.org/10.1016/j.jmatprotec.2015.11.016
24. A. Aversa, M. Moshiri, E. Librera, M. Hadi, G. Marchese, D. Manfredi, M. Lorusso, F. Calignano, S. Biamino, M. Lombardi and M. Pavese, Single Scan Track Analyses on Aluminium Based Powders, *J. Mater. Process. Technol.*, 2018, **255**, p 17–25. https://doi.org/10.1016/J.JMATPROTEC.2017.11.055
25. P. Wei, Z. Wei, Z. Chen, Y. He and J. Du, Thermal Behavior in Single Track During Selective Laser Melting of AlSi10Mg Powder, *Appl. Phys. A Mater. Sci. Process.*, 2017, **123**, p 1–13. https://doi.org/10.1007/s00339-017-1194-9
26. P. Wei, Z. Wei, Z. Chen, J. Du, Y. He, J. Li and Y. Zhou, The AlSi10Mg Samples Produced by Selective Laser Melting: Single Track, Densification, Microstructure and Mechanical Behavior, *Appl. Surf. Sci.*, 2017, **408**, p 38–50. https://doi.org/10.1016/J.APSUSC.2017.02.215
27. Z. Fan, M. Lu and H. Huang, Selective Laser Melting of Alumina: A Single Track Study, *Ceram. Int.*, 2018, **44**, p 9484–9493. https://doi.org/10.1016/J.CERAMINT.2018.02.166
28. R.M. Baitimerov, Single Track Formation During Selective Laser Melting of ti-6al-4v Alloy, *Mater. Sci. Forum.*, 2019, **946**, p 978–983. https://doi.org/10.4028/www.scientific.net/MSF.946.978
29. P.H. Shingu and K.N. Ishihara, Metastable Melting Phenomena and Solid State Amorphization (SSA) by Mechanical Alloying, *J. Alloys Compd.*, 1993, **194**, p 319–324. https://doi.org/10.1016/0925-8388(93)90017-H
30. H. M. Miekk-oja, Metallioppi, 3rd., Otava (1965)
31. J. Reijonen, A. Revuelta, T. Riipinen, K. Ruusuvuori and P. Puukko, On the Effect of Shielding Gas Flow on Porosity and Melt Pool Geometry in Laser Powder Bed Fusion Additive Manufacturing, *Addit. Manuf.*, 2020 https://doi.org/10.1016/j.addma.2019.101030
32. T. Nyyssönen, P. Peura and V.T. Kuokkala, Crystallography, Morphology and Martensite Transformation of Prior Austenite in Intercritically Annealed High-Aluminum Steel, *Metall Mater. Trans. A Phys. Metall. Mater. Sci.*, 2018, **49**, p 6426–6441. https://doi.org/10.1007/s11661-018-4904-9
33. Sten & Co Oy Ab, Hot work steel BÖHLER W302, Böhler W302 Datasheet. (n.d.)
34. J.J. Yan, D.L. Zheng, H.X. Li, X. Jia, J.F. Sun, Y.L. Li, M. Qian and M. Yan, Selective Laser Melting of H13: Microstructure and Residual Stress, *J. Mater. Sci.*, 2017, **52**, p 12476–12485. https://doi.org/10.1007/s10853-017-1380-3
35. M. Pérez, F.J. Belzunce, The Effect of Deep Cryogenic Treatments on the Mechanical Properties of an AISI H13 Steel, (2014). doi: https://doi.org/10.1016/j.msea.2014.11.051
36. A. Inoue and T. Masumoto, Carbide Reactions (M 3 C → M 7 C 3 → M 23 C 6 → M 6 C) During Tempering of Rapidly Solidified High Carbon Cr-W and Cr-Mo Steels, *Metall. Trans. A.*, 1980, **11**, p 739–747. https://doi.org/10.1007/BF02661203
37. H. Wang, J. Li, C. Bin Shi, J. Li and B. He, Evolution of Carbides in H13 Steel in Heat Treatment Process, *Mater. Trans.*, 2017, **58**, p 152–156. https://doi.org/10.2320/matertrans.M2016268
38. A. Ning, W. Mao, X. Chen, H. Guo and J. Guo, Precipitation Behavior of Carbides in H13 Hot Work Die Steel and its Strengthening During Tempering, *Metals (Basel).*, 2017, **7**, p 1–15. https://doi.org/10.3390/met7030070
39. J. Wilzer, Ã.J. Küpferle, S. Weber and W. Theisen, Influence of Alloying Elements, *Heat Treatment Temp. Thermal Conduct. Heat Treatable Steels*, 2015, **86**, p 1234–1241. https://doi.org/10.1002/srin.201400294
40. B. Cheng and K. Chou, A Numerical Investigation of Thermal Property Effects on Melt Pool Characteristics in Powder-Bed Electron Beam Additive Manufacturing, *Proc. Inst Mech. Eng. Part B J. Eng. Manuf.*, 2018, **232**, p 1615–1627. https://doi.org/10.1177/0954405416673105
41. S.H. Ahmed and A. Mian, Influence of Material Property Variation on Computationally Calculated Melt Pool Temperature During Laser Melting Process, *Metals (Basel).*, 2019 https://doi.org/10.3390/met9040456
42. J.C. Lippold, *Welding Metallurgy and Weldability*, 1st ed. John Wiley & Sons, New York, 2014
43. W.F. Savage, E.F. Nippes and M.C. Mushala, Liquid-Metal Embrittlement of the Heat-Affected Zone By Copper Contamination, *Weld. J. (Miami, Fla)*, 1978, **57**, p 237–245
44. M. Narvan, K.S. Al-Rubaie and M. Elbestawi, Process-Structure-Property Relationships of AISI H13 Tool Steel Processed with Selective Laser Melting, *Materials (Basel).*, 2019, **12**, p 2284. https://doi.org/10.3390/ma12142284
45. M. Åsberg, G. Fredriksson, S. Hatami, W. Fredriksson and P. Krakhmalev, Influence of Post Treatment on Microstructure, Porosity and Mechanical Properties of Additive Manufactured H13 Tool Steel, *Mater. Sci. Eng. A.*, 2019, **742**, p 584–589. https://doi.org/10.1016/J.MSEA.2018.08.046
46. H. Mehrer, *Diffusion in solids: Fundamentals, Methods, Materials, Diffusion-Controlled Processes*, Springer, Berlin, 2007. https://doi.org/10.1039/QR9702400601